CERN - EUROPEAN ORGANIZATION FOR NUCLEAR RESEARCH

Submitted to the
European Conf. on Particle Physics
Budapest, Hungary 4-9 July 1977

CERN/EP/PHYS 77-29
30 June 1977

ANALYSIS OF THE REACTION $\pi^- p \to \bar{p}pn$ AT 16 GeV/c

Bari-Bonn-CERN-Daresbury-Glasgow-Liverpool-Milano-Vienna Collaboration

C. EVANGELISTA, B. GHIDINI, A. PALANO, V. PICCIARELLI and G. ZITO
Istituto di Fisica dell'Università and INFN, Bari.

J. BRÖRING, P. MÄTTIG, K. MÜLLER, E. PAUL and W. RÜHMER
Physikalisches Institut der Universität, Bonn.

B.R. FRENCH, W.A. MITAROFF, C. PALAZZI-CERRINA, R. STRUB and A.S. THOMPSON(*)
CERN, European Organization for Nuclear Research, Geneva.

M. EDWARDS
Daresbury Physics Laboratory, Daresbury.

T. ARMSTRONG(**), J. GORDON, I.S. HUGHES, G.M. LEWIS and R.M. TURNBULL
University of Glasgow, Glasgow.

C. BEST, R.A. DONALD, D.N. EDWARDS and M.A. HOULDEN
Oliver Lodge Laboratory, University of Liverpool, Liverpool.

C. COSTA, L. MANDELLI and S. PENSOTTI
Istituto di Fisica dell'Università and INFN, Milano.

H.D. LAMBACHER(**)
Institut für Hochenergiephysik der Österreichischen Akademie der Wissenschaften, Vienna.

(*) Now at Glasgow.

(**) Now at CERN.

RS/ed

CERN/EP/PHYS 77-29

ABSTRACT

A sample of about $2 \cdot 10^4$ events $\pi^- p \to \bar{p}pn$ with peripherally produced $(\bar{p}p)$ or $(\bar{p}n)$ pairs has been obtained in the CERN Omega Spectrometer, using a 16 GeV/c π^- beam and triggering for a forward going $\bar{p}$. We present mass distributions, cross sections, and analyse the decay angular distributions for the $(\bar{p}p)$ and $(\bar{p}n)$ systems. While reaction $\pi^- p \to (\bar{p}p)n$ is consistent with the predictions of the O.P.E. model, the reaction $\pi^- p \to (\bar{p}n)p$ requires a more complex exchange mechanism.

1. INTRODUCTION

We present data on the reaction

$$\pi^- p \to \bar{p}pn \qquad (1)$$

and on the subchannels,

$$\pi^- p \to (\bar{p}p)n \qquad (2)$$

and

$$\pi^- p \to (\bar{p}n)p \qquad (3)$$

at 16 GeV/c, using the CERN Omega spectrometer. The experimental layout, trigger and data handling procedure are described in sect. 2, and in sect. 3 we present the effective mass distributions and cross sections for reactions (2) and (3). In sect. 4 we show the decay angular distributions and mean values of the spherical harmonics as a function of the nucleon-antinucleon mass.

2. EXPERIMENTAL TECHNIQUES

The experiment was performed on the Omega spectrometer [1] using the layout shown in fig. 1, with a 16 GeV/c unseparated negative beam. The incident pions were identified by means of three Cerenkov counters. A system of Multiwire Proportional Chambers (MWPC) allowed the measurement of their direction with an accuracy of $\delta\lambda = \delta\phi = \pm 0.2$ mrad, and of their momentum with $\delta p/p = \pm 0.9\%$.

The selection of events by the trigger required:

(a) An interaction in the 30 cm liquid H_2 target as defined by either a hit in the scintillation counter (TS) around the target, or at least two hits in MWPC I just downstream of the target.

(b) A hit in MWPC II.

(c) No hit in the beam particle veto counter V.

(d) A hit in scintillation hodoscope H_1 correlated to a hit in the scintillation hodoscope H_2.

(e) No light in the atmospheric pressure Cerenkov counter C_1 filled with isobutane, which had π^-, K^- and $\bar{p}$ thresholds of 2.8, 9.8 and 18.8 GeV/c, respectively.

The trigger was thus designed to accept those interactions in the H_2 target producing a forward going K^- with momentum between 2.8 and 9.8 GeV/c, or a $\bar{p}$ with momentum greater than 2.8 GeV/c.

The second Cerenkov counter C_2 was filled with freon-13 at 5.4 atmosphere absolute pressure and allowed tagging of kaons and antiprotons (protons) between 5 and 10 GeV/c. The information from the Cerenkov counter C_2 was used in this analysis to check the contamination by kaons in reaction (1) from the competing reactions

$$\pi^- p \to K^- K^+ n \qquad (4)$$

and

$$\pi^- p \to K^- K^o p \quad . \qquad (5)$$

In total 1.2 million triggers were recorded, corresponding to a beam flux sensitivity of 2400 events/μb.

The total sample of triggered events was processed through an adapted version of the Omega pattern recognition and geometry program ROMEO [2]. Fig. 2 shows the distribution of the missing mass for all reconstructed two-prong events with a good traced trigger track, and with $\bar{p}$, p assignment for the charged particles. There is a clear signal of a missing neutron for reaction (1), with FWHM of 230 MeV. If we assume K^+, K^- assignment of the charged tracks the neutron peak becomes less pronounced and broadens to about 380 MeV, indicating that the number of $\bar{p}pn$ events is larger than the number of K^+K^-n events. In the corner of fig. 1 we show the missing mass distribution calculated under the assumption of K^-, p assignment for the charged tracks. No accumulation around the K^o mass is visible. The accumulation of events with a missing mass larger than 1.4 GeV is due to reactions with multineutral production. The cross hatched histogram under the missing mass spectrum represents the sample where the triggering particle was positively identified as an antiproton (of momentum greater than 9.8 GeV/c) by Cerenkov C_1.

The reconstructed events were processed using a modified version of the kinematics program KOMEGA [3], and channel (1) was selected by demanding a fit probability greater than 0.1. The final data sample consisted of 19 389 events, of which we estimate from the Cerenkov (C_2) information that $\sim$ 10% is contamination from kaon hypotheses. The data were corrected for two kinds of correlated losses, namely: (a) geometrical losses due to the beam particle veto counter and the finite angular acceptance of Cerenkov (C_1) for the trigger particle, and (b) charged particle detection losses for low momentum particles. The inability to detect low momentum protons restricted our analysis to the four-momentum transfer range $|t_{pp}| > 0.09$ (GeV/c)^2.

3. EFFECTIVE MASS DISTRIBUTIONS AND CROSS SECTIONS

Figs 3 and 4 show the weighted and unweighted $(\bar{p}p)$ and $(\bar{p}n)$ effective mass spectra for all events. From these two figures we see that reaction (1) is produced either with a peripheral $(\bar{p}p)$ system or a peripheral $(\bar{p}n)$ system. The accumulation of events with an effective mass greater than 3.2 GeV visible in the $\bar{p}p$ distribution of fig. 3 is due to the kinematical reflection of the low mass $(\bar{p}n)$ system shown in fig. 4, and vice versa.

The two-dimensional plot (not shown) of the four-momentum transfers, $|t_{pp}|$ versus $|t_{np}|$, shows strong accumulations for both low $|t_{pp}|$ and low $|t_{np}|$ values, which suggests a method for separating the two peripheral mechanism $\pi^- p \to (\bar{p}p)n$ and $\pi^- p \to (\bar{p}n)p$ by ascribing the lower value of the four-momentum transfer to the recoil particle.

In fig. 5 we display the effective mass distribution of the $(\bar{p}p)$ and $(\bar{p}n)$ systems using the four-momentum transfer selection, and after correcting for kaon contamination. For the reaction $\pi^- p \to (\bar{p}n)p$ we also apply a cut on the four-momentum transfer to the proton due to our inability to make complete corrections for $|t_{pp}| < 0.09$ (GeV/c)^2. No such cut is needed for the $(\bar{p}p)n$ data. The mass resolution, σ, for this data is typically 8 MeV for the $(\bar{p}p)$ system and 18 MeV for the $(\bar{p}n)$ system over the effective mass range from threshold up to 2.5 GeV.

The cross sections for the reaction channels (2) and (3) are given in table 1.

In table 2 we present measured values for the slopes of the differential cross sections for reactions $\pi^- p \to (\bar{p}p)n$ and $\pi^- p \to (\bar{p}n)p$ in different intervals of the nucleon-antinucleon effective mass, evaluated by fitting the reduced four-momentum transfer distribution, $t' = |t| - t_{min}$, with an exponential function of the form $Ae^{-bt'}$ over the range $0.09 \leq t' \leq 0.39$ $(GeV/c)^2$.

We note that the values of b for the two reactions are substantially independent of the effective mass, and appear to be consistent with each other.

4. DECAY ANGULAR DISTRIBUTIONS AND SPHERICAL HARMONIC MOMENTS

Figs 6 and 7 show the unweighted (full line) and acceptance-corrected (points with error bars) decay angular distributions of the $(\bar{p}p)$ and $(\bar{p}n)$ systems, respectively, in the Gottfried-Jackson reference frame for eight different effective mass intervals from 1.9 to 3.2 GeV. The angles θ and ϕ are defined relative to the antiproton direction. We see rapid, but similar, variation in the structure of $\cos\theta$ for the two systems up to 2.2 GeV, that is to say a sharp backward peak and an accumulation of events near $\cos\theta = 0$. In the mass region from 2.2 to 2.6 GeV the $(\bar{p}p)$ distribution clusters around $\cos\theta \approx 0$ with an indication of a forward peak at high mass, while on the contrary the $(\bar{p}n)$ system tends to decay symmetrically. For masses higher than 2.6 GeV the $(\bar{p}p)$ system is strongly asymmetric, peaking towards the forward direction, while the $(\bar{p}n)$ system shows approximate forward and backward symmetry. Whereas an almost flat distribution of the Treiman-Yang angle, ϕ, is observed in all mass intervals for the $(\bar{p}p)$ system, compatible with one pion exchange, the same is not true for the $(\bar{p}n)$ system, suggesting that a more complex exchange mechanism is needed.

In figs 8-11 we present normalized spherical harmonic moments, $\langle Y_\ell^m \rangle$, for the $(\bar{p}p)$ and $(\bar{p}n)$ systems for values of ℓ from 1 to 10 and m of 0 and 1, as a function of the nucleon-antinucleon effective mass from 1.9 to 2.5 GeV. At large effective masses the calculated moments will be progressively distorted by increasing regions of zero acceptance in the decay angular distributions, but no such regions exist below 2.3 GeV. In order to reduce the contamination from kaon events, which we believe mainly affects the $\langle Y_4^0 \rangle$ moment via production of the A_2 and f resonances, we have restricted the analysis to those $(\bar{p}p)n$ events where the missing mass to the $(\bar{p}p)$ system is greater than 0.88 GeV. This reduces the contamination in the $(\bar{p}p)n$ channel from 10% to 3%.

Figs 8(a)-11(a) display moments for the above defined sample of $(\bar{p}p)n$ events, while figs 8(b)-11(b) represent a subsample of these $(\bar{p}p)n$ events with four-momentum transfer $|t_{np}| > 0.09$ (GeV/c)^2, in order to enable comparison with the $(\bar{p}n)p$ data of figs 8(c)-11(c) where the restriction $|t_{pp}| > 0.09$ (GeV/c)^2 is due to the loss of low momentum protons, as discussed in sect. 2.

In general there appears to be more structure in the $(\bar{p}p)$ moments than in the $(\bar{p}n)$, but we note that this difference diminishes when the cut on momentum transfer is imposed also on the $(\bar{p}p)n$ data. All the $\langle Y_\ell^1 \rangle$ moments are consistent with zero for the $(\bar{p}p)$ system, while the $\langle Y_1^1 \rangle$ and $\langle Y_4^1 \rangle$ moments are not compatible with zero for the $(\bar{p}n)$ system. A strong variation in intensity with mass of the $\langle Y_2^0 \rangle$ moment is apparent in both reactions. By contrast, the signal evident in the $\langle Y_6^0 \rangle$ moment of the $(\bar{p}p)$ system at a mass of 2.10 GeV is not apparent in the $(\bar{p}n)$ system. However, the diminished significance of this signal in the $(\bar{p}p)$ data when events with $|t_{np}| < 0.09$ (GeV/c)^2 are excluded suggests some dependence on the four-momentum transfer. Our $(\bar{p}p)n$ data show good agreement with that of Hyams et al. [4] except for some differences in the $\langle Y_2^0 \rangle$ and $\langle Y_4^0 \rangle$ moments. We should also like to draw attention to the behaviour of the $\langle Y_4^0 \rangle$ and $\langle Y_4^1 \rangle$ moments in the $(\bar{p}n)$ data. While we cannot exclude the possibility that part of this structure is due to kaon contamination, we think it unlikely that the whole structure can be explained in this way.

5. CONCLUSION

We have analysed the reactions $\pi^- p \to (\bar{p}p)n$ and $\pi^- p \to (\bar{p}n)p$ and find the cross sections to be

$$\sigma(\bar{p}p) = 2.7 \pm .25 \ \mu b; \qquad \sigma(\bar{p}n) = 4.6 \pm .5 \ \mu b,$$

within the kinematical limits of the nucleon-antinucleon effective mass from threshold up to 2.3 GeV, and the four-momentum transfer region $|t_{NN}| > 0.09$ $(GeV/c)^2$.

We have presented a comparison of the decay angular distributions and the spherical harmonic moments for the two channels, and for existing $(\bar{p}p)n$ data. We have mentioned interesting structures in some of the $\langle Y_\ell^m \rangle$ moments, but a detailed interpretation will require an amplitude analysis.

REFERENCES

[1] O. Gildermeister, Int. Conf. on Instrumentation for High Energy Physics, Frascati 1973.

[2] F. Bourgeois, H. Grote and J.C. Lassalle, Pattern Recognition Methods for Omega and SFM Spark Chamber Experiments, CERN DD/DH 70-13.

H. Grote, M. Hansroul, J.C. Lassalle and P. Zanella, Identification of Digitised Particle Trajectories, Int. Computing Symposium 1973 (North Holland, 1973).

[3] CERN Hydra Application Library.

[4] B. Hyams et al., Peripheral $p\bar{p}$ Production and Decay Angular Distribution in the Reaction $\pi^- p \to ppn$ at 18.8 and 9.8 GeV, Nucl. Phys. B73 (1974) 202.

Table 1

The zero acceptance regions in the mass range (2.3 - 3.2 GeV) have been corrected on the basis of isotropic angular decay distributions.

Final state	Mass Interval (GeV)	Cross section (μb) $\|t_{NN}\| > 0$	Cross section (μb) $\|t_{NN}\| > 0.09$
$(\bar{p}p)n$	1.87 - 2.30	3.8 ± .3	2.7 ± .25
	1.87 - 3.20	6.5 ± .7	4.4 ± .5
$(\bar{p}n)p$	1.87 - 2.30		4.6 ± .5
	1.87 - 3.20		7.8 ± .9

Table 2

Mass Interval GeV	Slope Parameter b $\pi^- p \to (\bar{p}p)n$	Slope Parameter b $\pi^- p \to (\bar{p}n)p$
1.9 - 2.0	5.9 ± 0.6	6.9 ± 0.6
2.0 - 2.1	5.9 ± 0.5	6.4 ± 0.5
2.1 - 2.2	7.0 ± 0.5	5.1 ± 0.5
2.2 - 2.3	6.5 ± 0.6	6.2 ± 0.5
2.3 - 2.4	8.0 ± 0.6	5.4 ± 0.7
2.4 - 2.6	6.8 ± 0.5	5.9 ± 0.6

FIGURE CAPTIONS

Fig. 1 Layout of the Omega spectrometer and trigger equipment used in the present experiment.

Fig. 2 Missing mass distribution for reconstructed two-prong events with a good traced trigger track and the mass assignment of $\bar{p}$, p for the charged particles. The hatched distribution is for the sample with positively identified antiproton, while the inset distribution is for a charged particle assignment of K^-, p.

Fig. 3 Effective mass distribution of the $\bar{p}p$ combination for all events. The dotted curve shows the unweighted events while the full curve shows the events corrected for acceptance.

Fig. 4 Effective mass distribution of the $\bar{p}n$ combination for all events. The dotted curve shows the unweighted events while the full curve shows the events corrected for acceptance.

Fig. 5 (a) Effective mass distribution of the $(\bar{p}p)$ system with $|t_{np}| < |t_{pp}|$, given in terms of events per mass interval and μbarn per mass interval.

(b) Effective mass distribution of the $(\bar{p}n)$ system with $|t_{pp}| < |t_{np}|$ and $|t_{pp}| > 0.09$ $(GeV/c)^2$, given in terms of events per mass interval and μbarn per mass interval.

The arrows indicate the limits of the zero acceptance region.

Fig. 6 Decay angular distributions for the $(\bar{p}p)$ system:

(a) $M(\bar{p}p)$ from threshold up to 2.3 GeV;

(b) $2.3 \leq M(\bar{p}p) \leq 3.2$ GeV.

The arrow indicates the limit of the zero acceptance region.

FIGURE CAPTIONS (Cont'd)

Fig. 7 Decay angular distributions of the $(\bar{p}n)$ system with $|t_{np}| > 0.09$ (GeV/c)^2:

(a) $M(\bar{p}n)$ from threshold up to 2.3 GeV;

(b) $2.3 \leqslant M(\bar{p}n) \leqslant 3.2$ GeV.

The arrow indicates the limit of the zero acceptance region.

Fig. 8 Normalized spherical harmonic moments $\langle Y_\ell^0 \rangle$ for $1 \leqslant \ell \leqslant 5$ for antinucleon-nucleon mass from threshold up to 2.5 GeV. (a) $(\bar{p}p)n$, (b) $(\bar{p}p)n$ with $|t_{np}| > 0.09$ (GeV/c)^2, (c) $(\bar{p}n)p$ with $|t_{pp}| > 0.09$ (GeV/c)^2.

Fig. 9 As in fig. 8 for $\langle Y_\ell^0 \rangle$ with $6 \leqslant \ell \leqslant 10$.

Fig. 10 As in fig. 8 for $\langle Y_\ell^1 \rangle$ with $1 \leqslant \ell \leqslant 5$.

Fig. 11 As in fig. 8 for $\langle Y_\ell^1 \rangle$ with $6 \leqslant \ell \leqslant 10$.

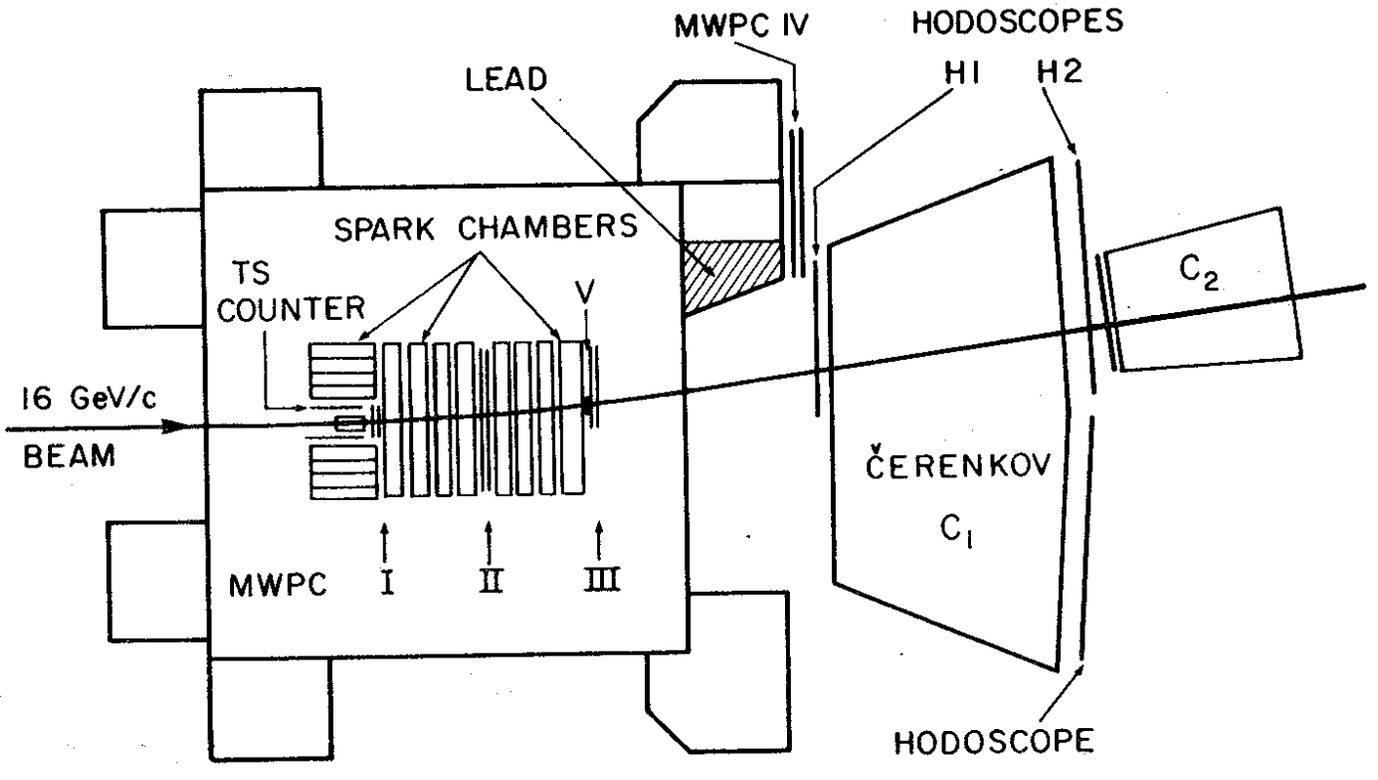
MWPC IV
HODOSCOPES
H1
H2
LEAD
SPARK CHAMBERS
TS
COUNTER
V
C2
16 GeV/c
BEAM
ČERENKOV
C1
MWPC
I
II
III
HODOSCOPE

Fig. 1

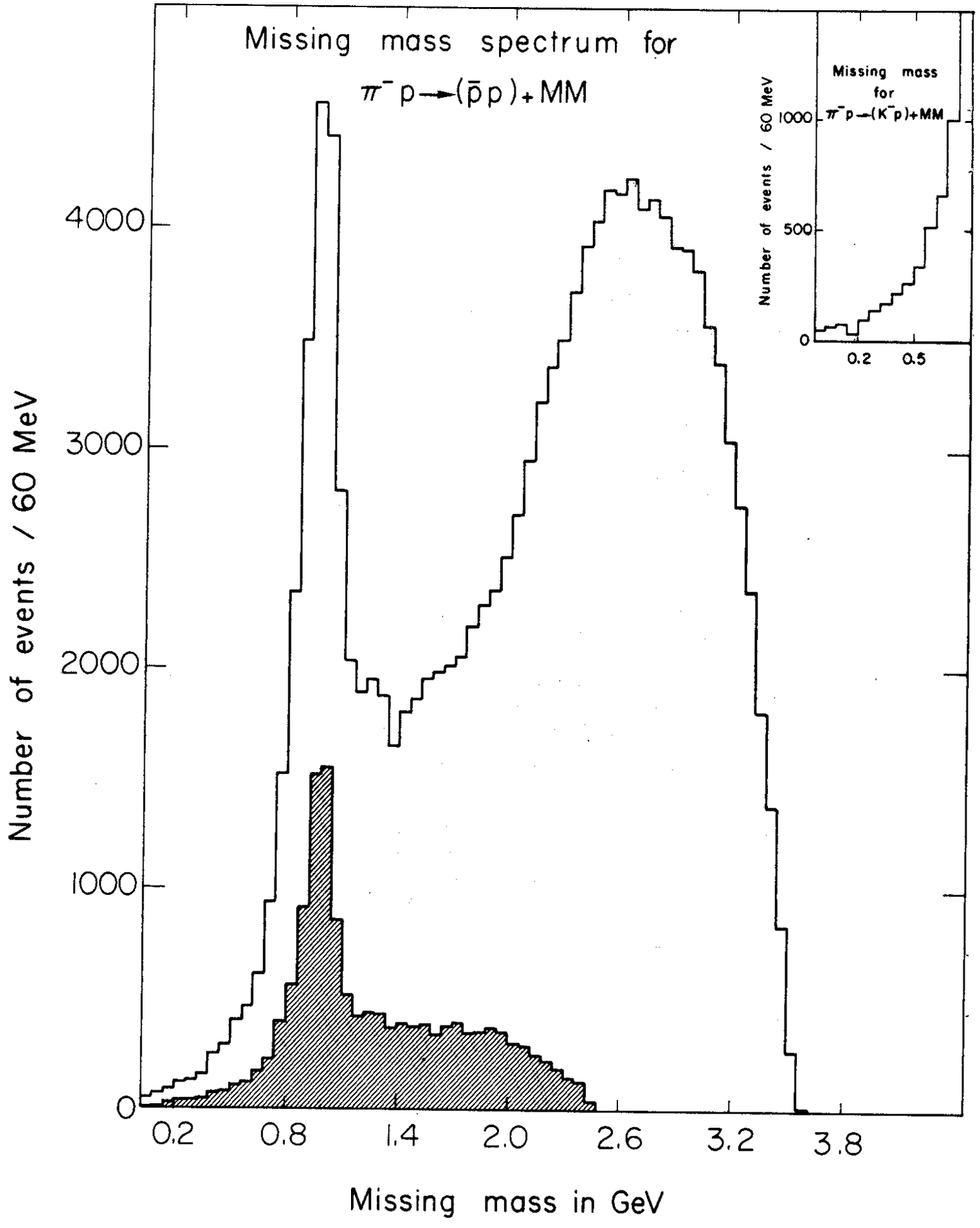
Missing mass spectrum for
$\pi^- p \rightarrow (\bar{p}p) + MM$
Missing mass for $\pi^- p \rightarrow (K^- p) + MM$
Number of events / 60 MeV
Missing mass in GeV
0
1000
2000
3000
4000
0.2
0.8
1.4
2.0
2.6
3.2
3.8
500
0.5

Fig. 2

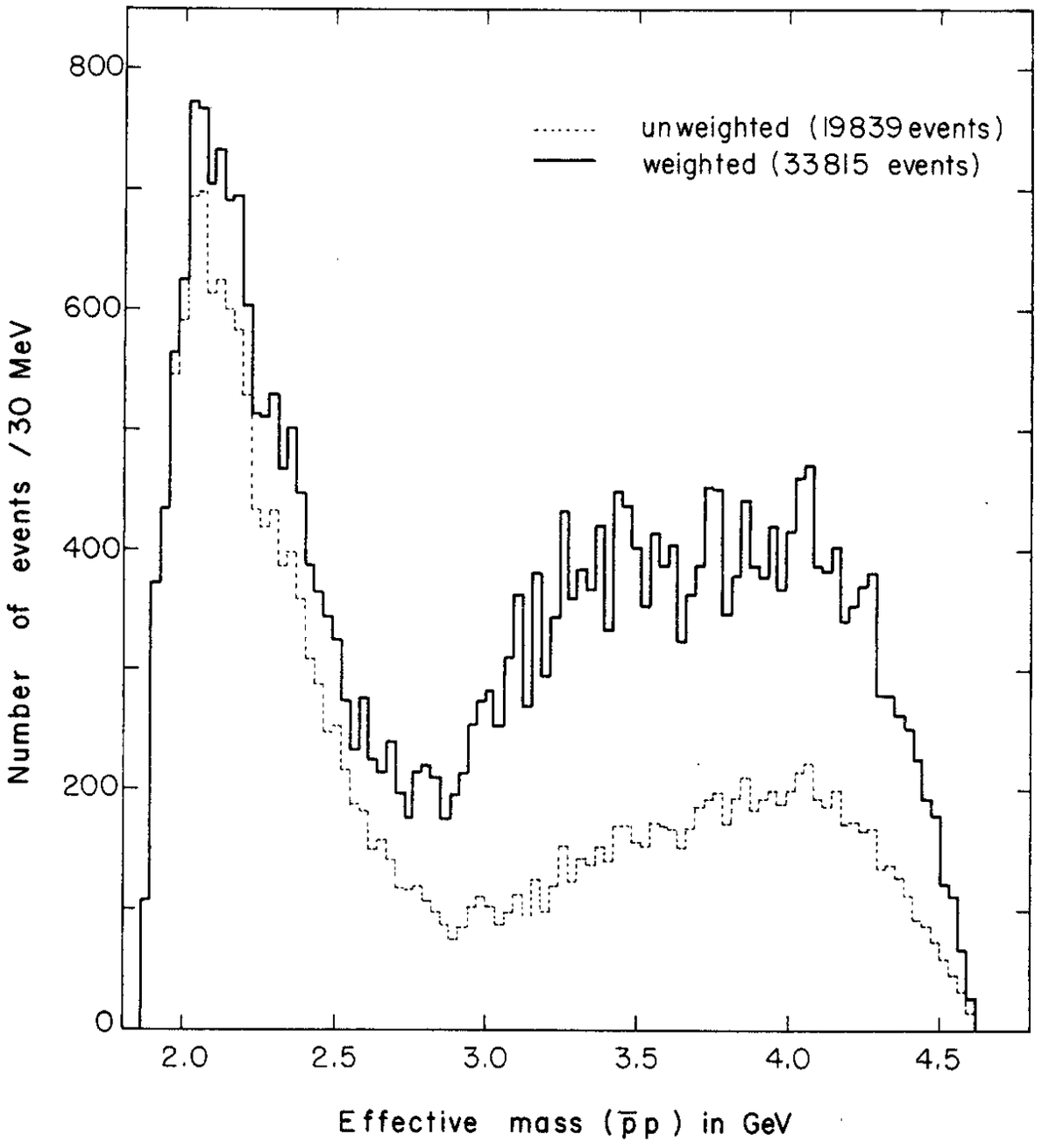
800
600
400
200
0
Number of events /30 MeV
unweighted (19839 events)
weighted (33815 events)
2.0
2.5
3.0
3.5
4.0
4.5
Effective mass ($\bar{p}p$) in GeV

Fig. 3

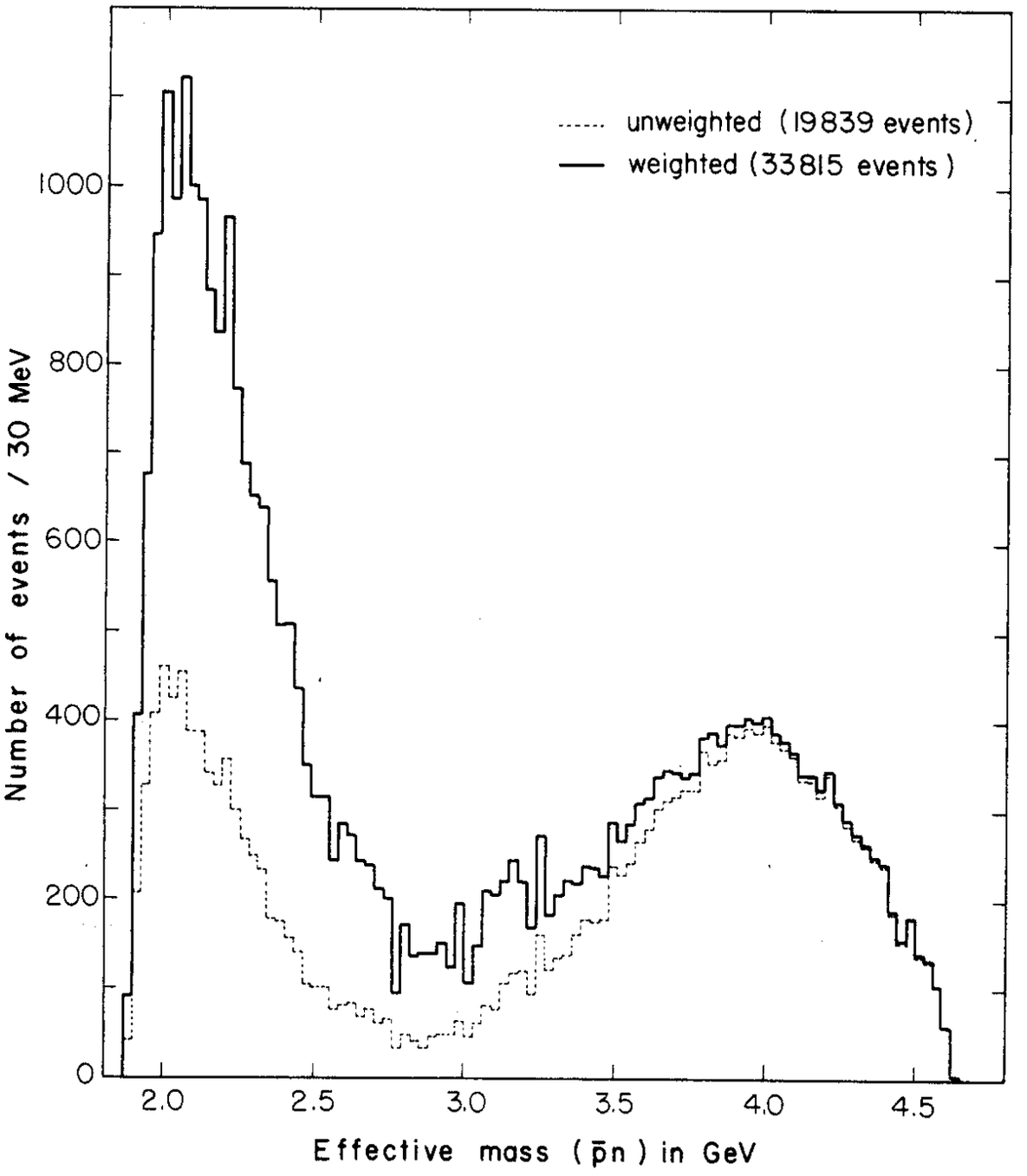
unweighted (19839 events)
weighted (33815 events)
Number of events / 30 MeV
0
200
400
600
800
1000
2.0
2.5
3.0
3.5
4.0
4.5
Effective mass ($\bar{p}n$) in GeV

Fig. 4

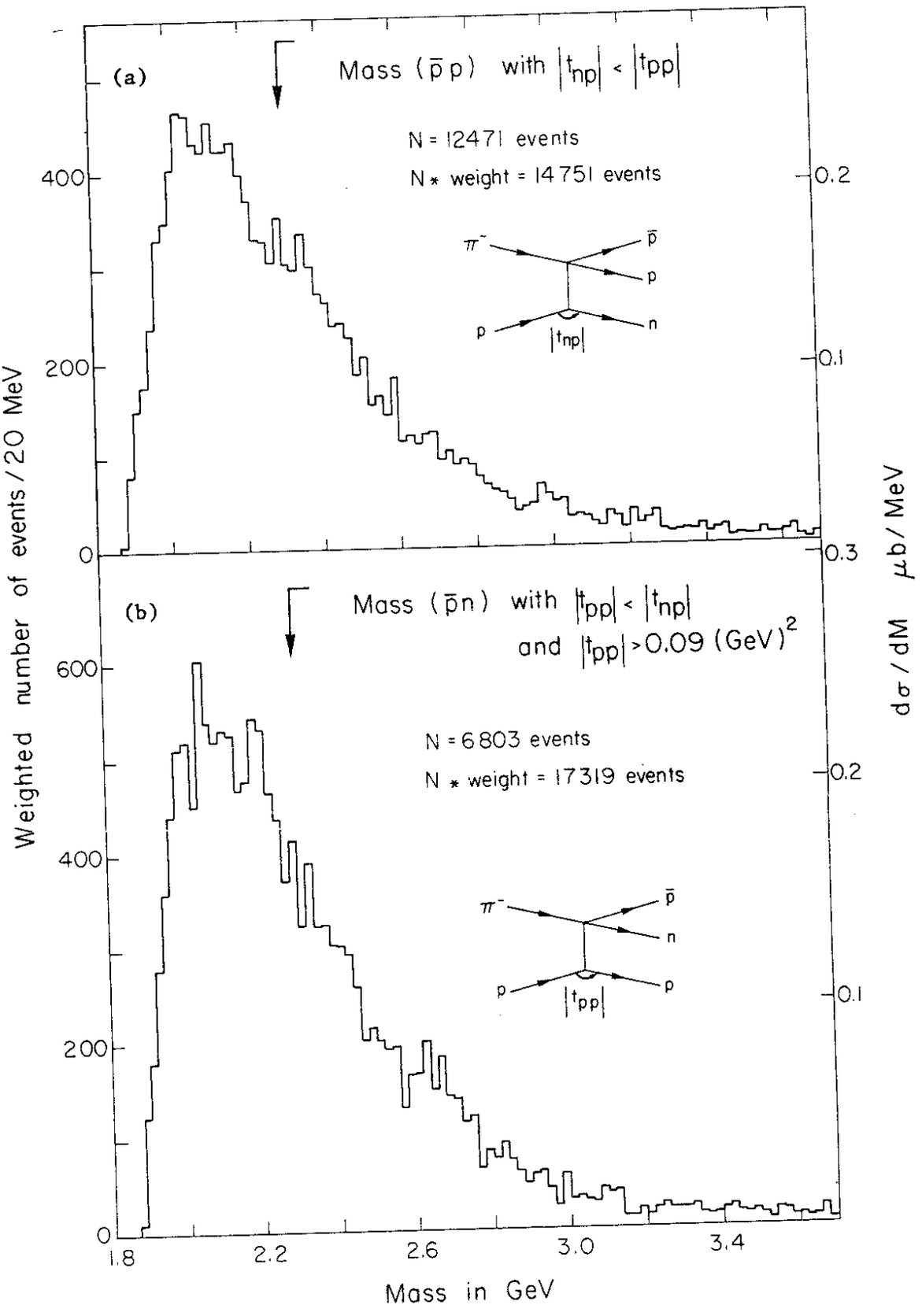
(a)
Mass ($\bar{p}$p) with $|t_{np}| < |t_{pp}|$
N = 12471 events
N * weight = 14751 events
π^-
$\bar{p}$
p
p
n
$|t_{np}|$
(b)
Mass ($\bar{p}$n) with $|t_{pp}| < |t_{np}|$
and $|t_{pp}| > 0.09$ (GeV)^2
N = 6803 events
N * weight = 17319 events
π^-
$\bar{p}$
n
p
p
$|t_{pp}|$
Weighted number of events / 20 MeV
dσ / dM μb / MeV
Mass in GeV
0
200
400
600
0.1
0.2
0.3
1.8
2.2
2.6
3.0
3.4

Fig. 5

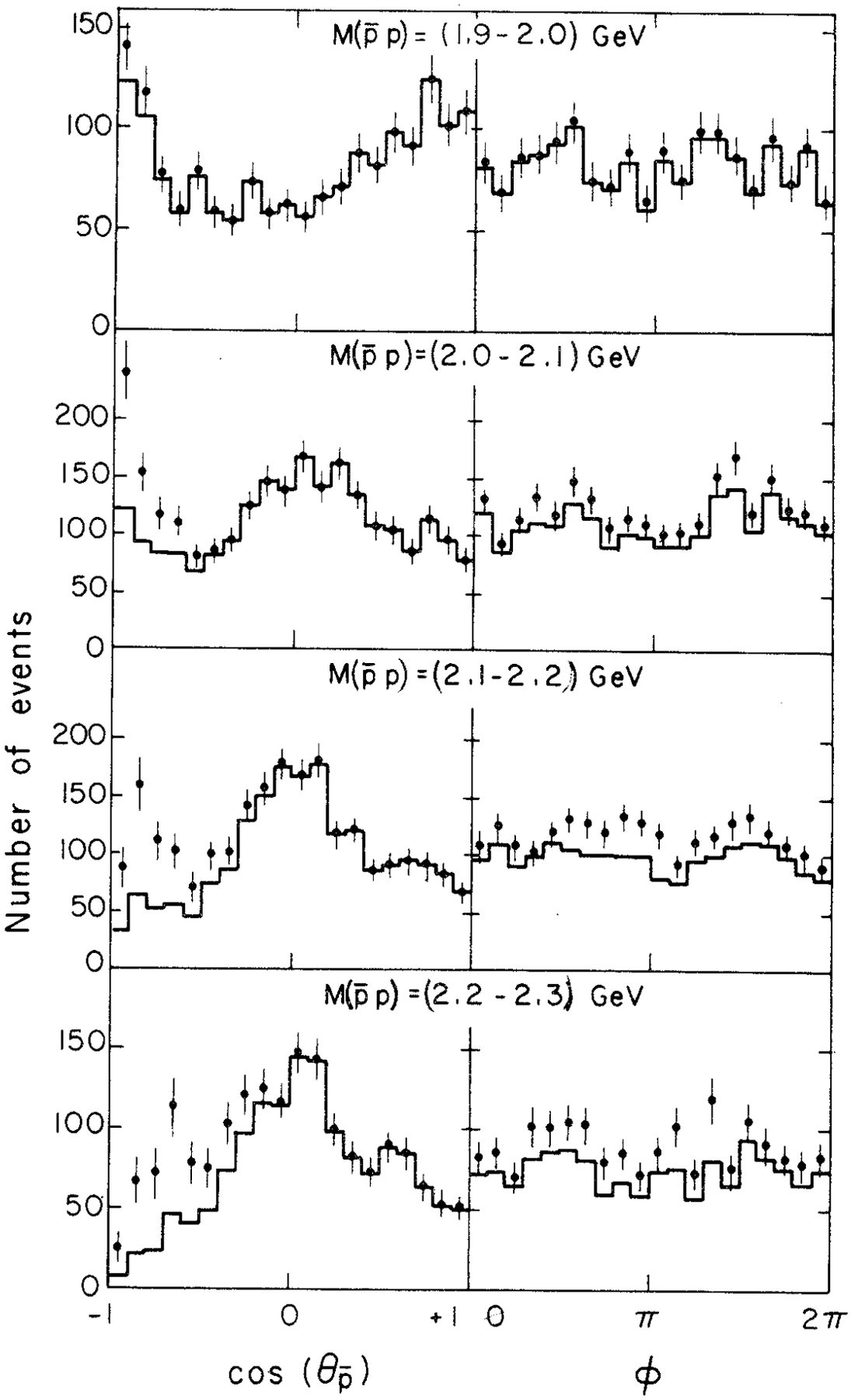
M(p̄ p) = (1.9 - 2.0) GeV
M(p̄ p) = (2.0 - 2.1) GeV
M(p̄ p) = (2.1 - 2.2) GeV
M(p̄ p) = (2.2 - 2.3) GeV
Number of events
cos (θp̄)
φ
-1
0
+1
0
π
2π

Fig. 6(a)

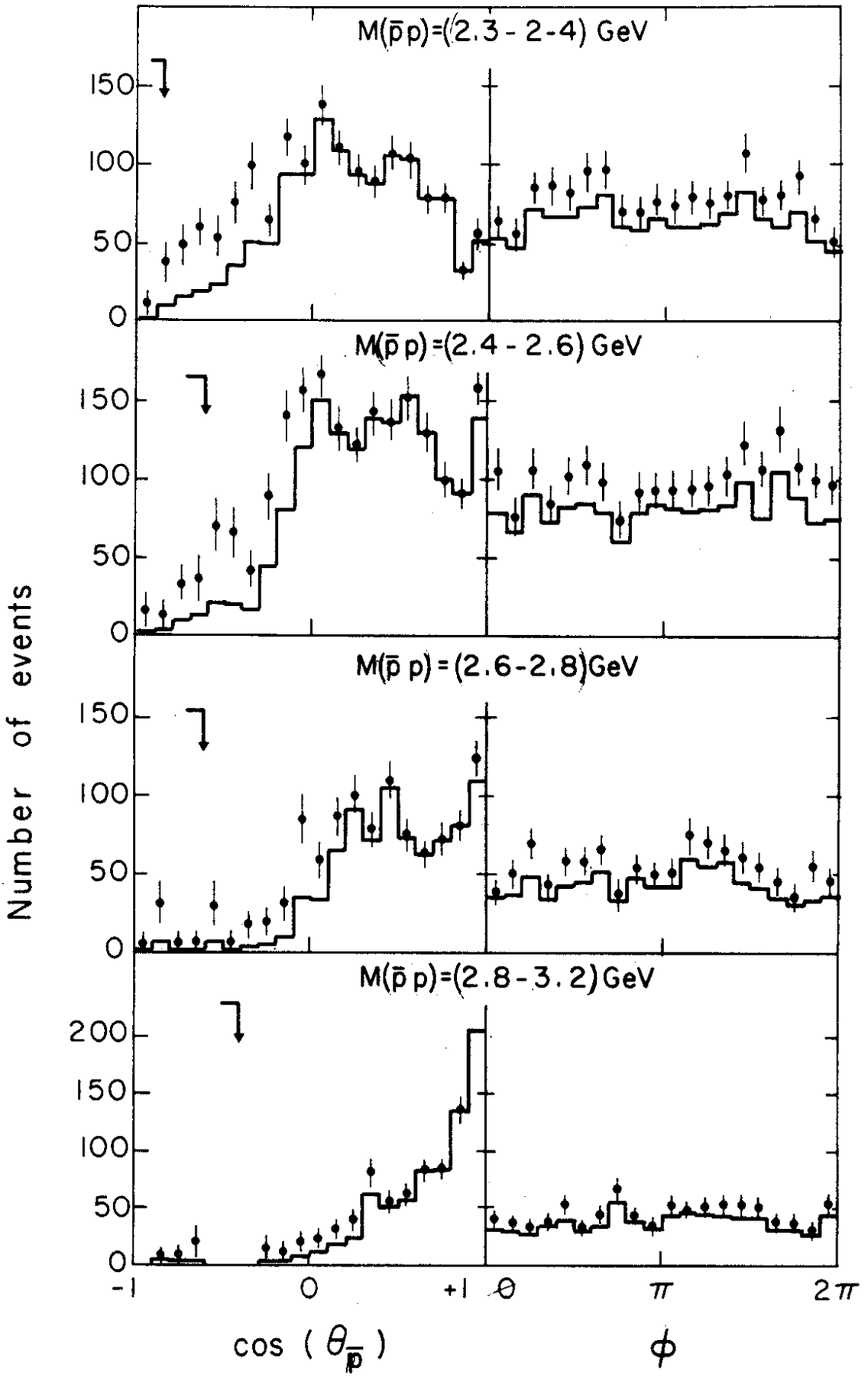
M(p̄p)=(2.3 - 2-4) GeV
M(p̄ p)=(2.4 - 2.6) GeV
M(p̄ p) = (2.6-2.8)GeV
M(p̄ p)=(2.8-3.2)GeV
Number of events
150
100
50
0
200
-1
0
+1
θ
π
2π
cos (θ p̄)
φ

Fig. 6(b)

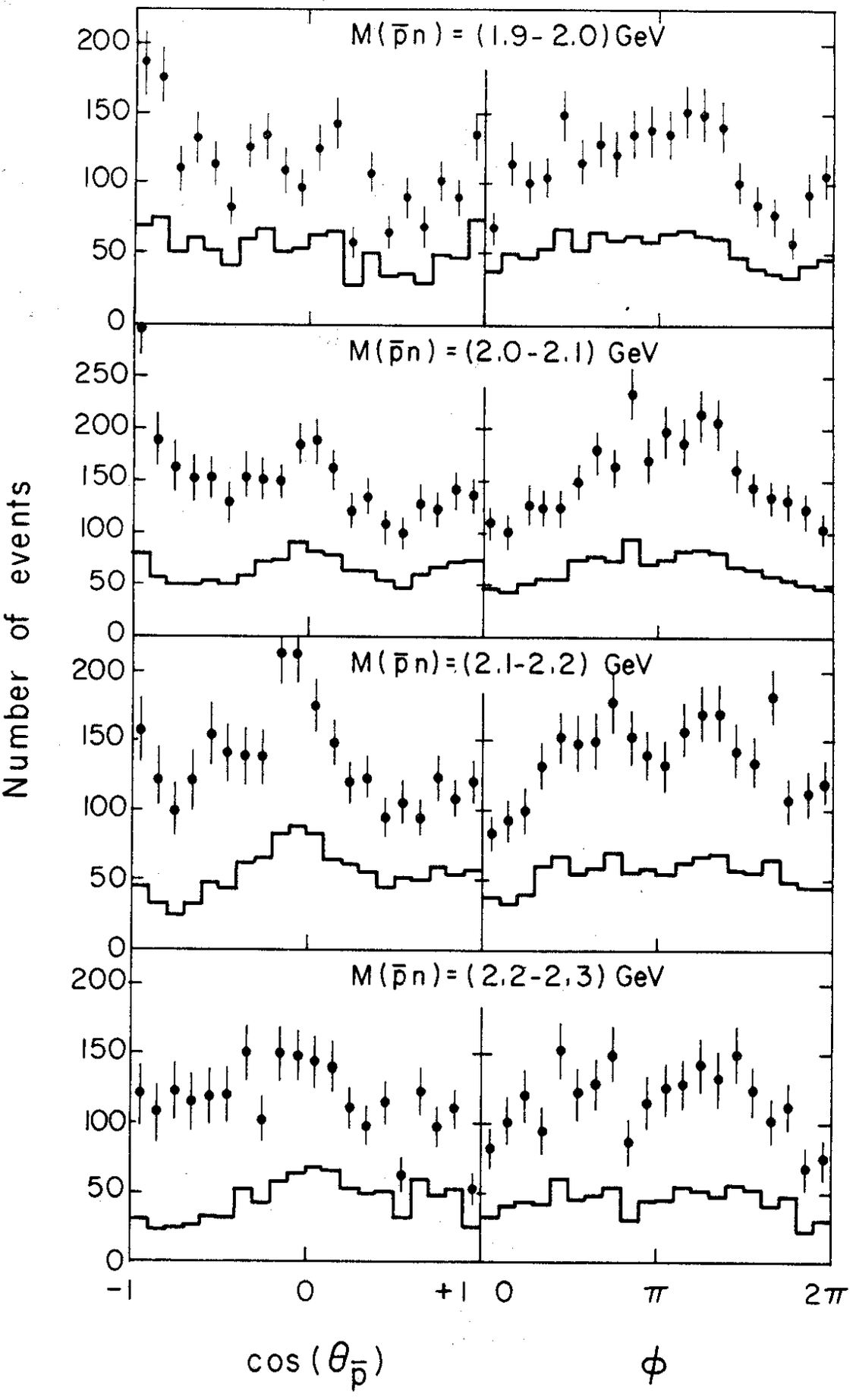
M(p̄n) = (1.9 - 2.0) GeV
M(p̄n) = (2.0 - 2.1) GeV
M(p̄n) = (2.1-2.2) GeV
M(p̄n) = (2.2-2.3) GeV
Number of events
cos (θp̄)
φ
-1
0
+1
0
π
2π

Fig. 7(a)

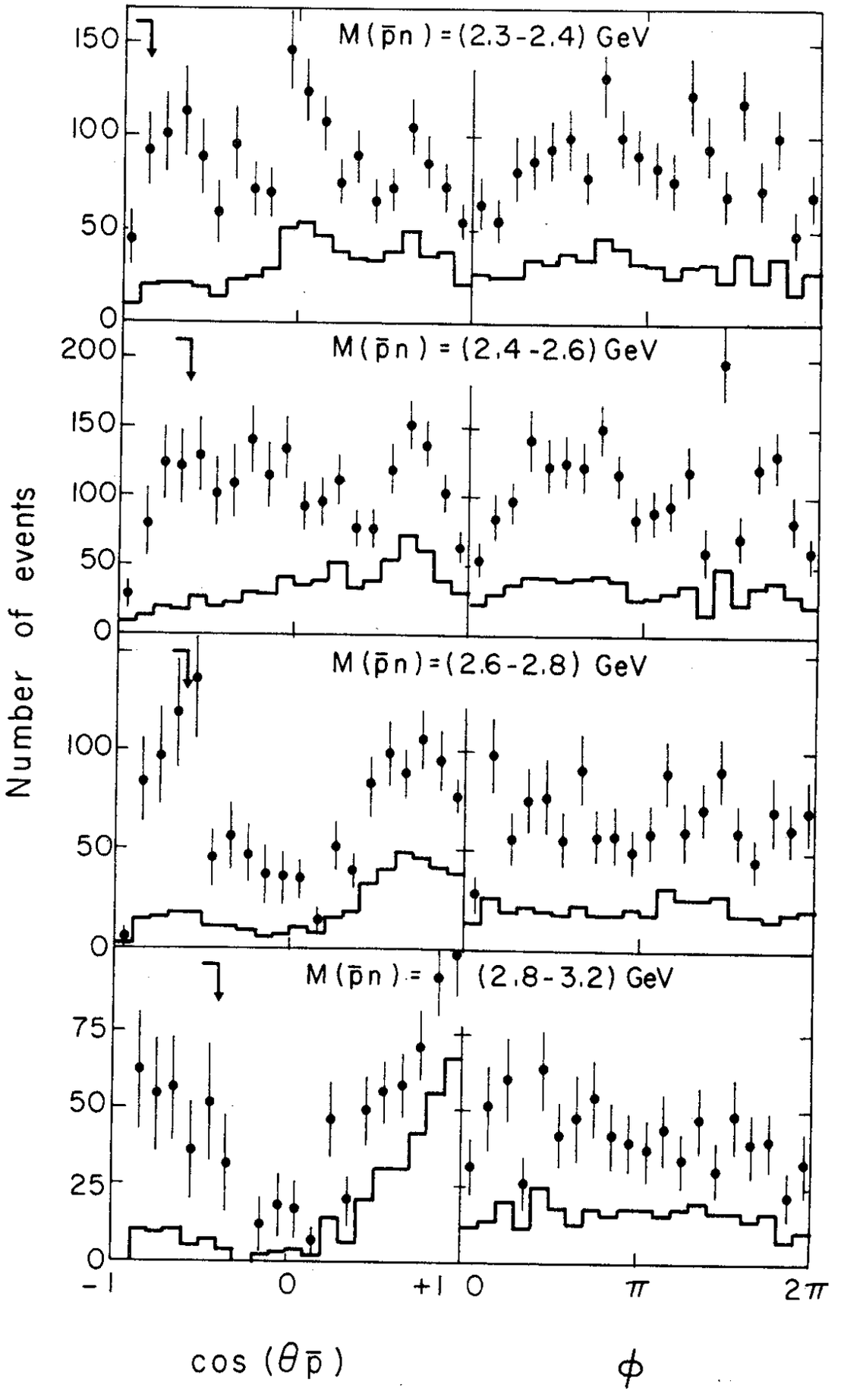
M(p̄n) = (2.3-2.4) GeV
M(p̄n) = (2.4-2.6) GeV
M(p̄n) = (2.6-2.8) GeV
M(p̄n) = (2.8-3.2) GeV
Number of events
cos (θp̄)
φ

Fig. 7(b)

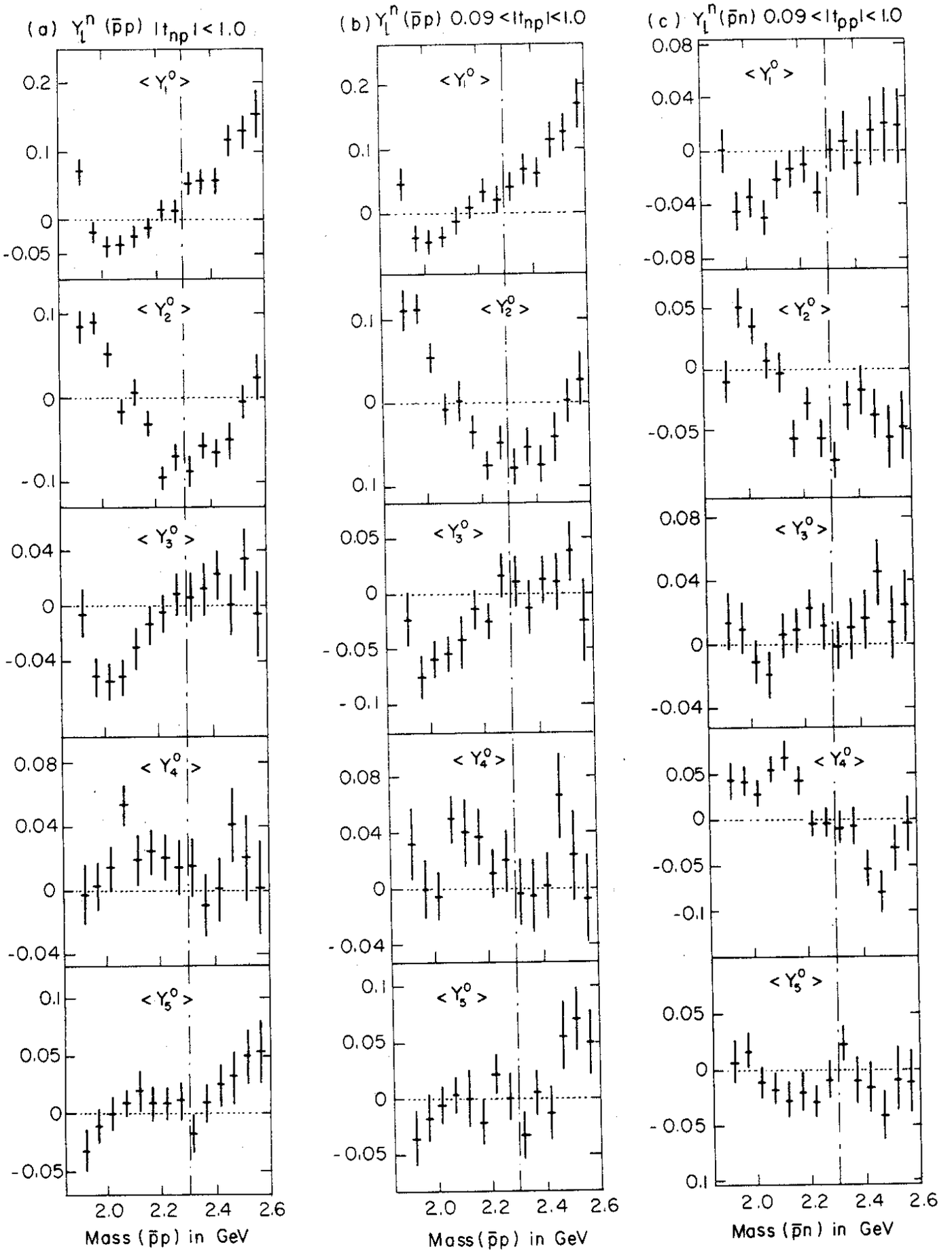
(a) Y_l^n $(\bar{p}p)$ $|t_{np}|<1.0$
(b) Y_l^n $(\bar{p}p)$ $0.09<|t_{np}|<1.0$
(c) Y_l^n $(\bar{p}n)$ $0.09<|t_{pp}|<1.0$
$<Y_1^0>$
$<Y_2^0>$
$<Y_3^0>$
$<Y_4^0>$
$<Y_5^0>$
Mass $(\bar{p}p)$ in GeV
Mass $(\bar{p}p)$ in GeV
Mass $(\bar{p}n)$ in GeV

Fig. 8

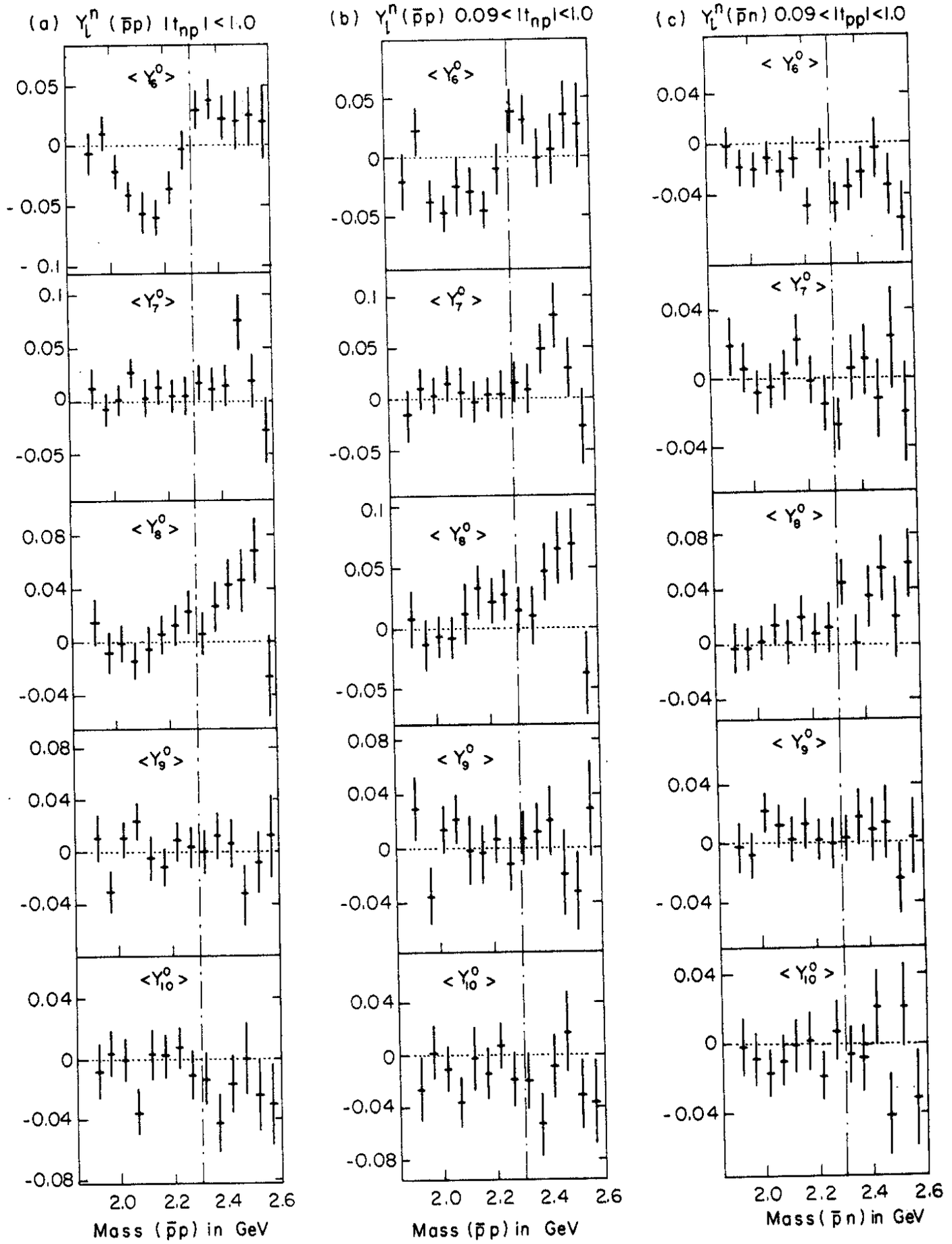
(a) Y_L^n ($\bar{p}p$) $|t_{np}|<1.0$
(b) Y_L^n ($\bar{p}p$) $0.09<|t_{np}|<1.0$
(c) Y_L^n ($\bar{p}n$) $0.09<|t_{pp}|<1.0$
$\langle Y_6^0 \rangle$
$\langle Y_7^0 \rangle$
$\langle Y_8^0 \rangle$
$\langle Y_9^0 \rangle$
$\langle Y_{10}^0 \rangle$
Mass ($\bar{p}p$) in GeV
Mass ($\bar{p}p$) in GeV
Mass ($\bar{p}n$) in GeV

Fig. 9

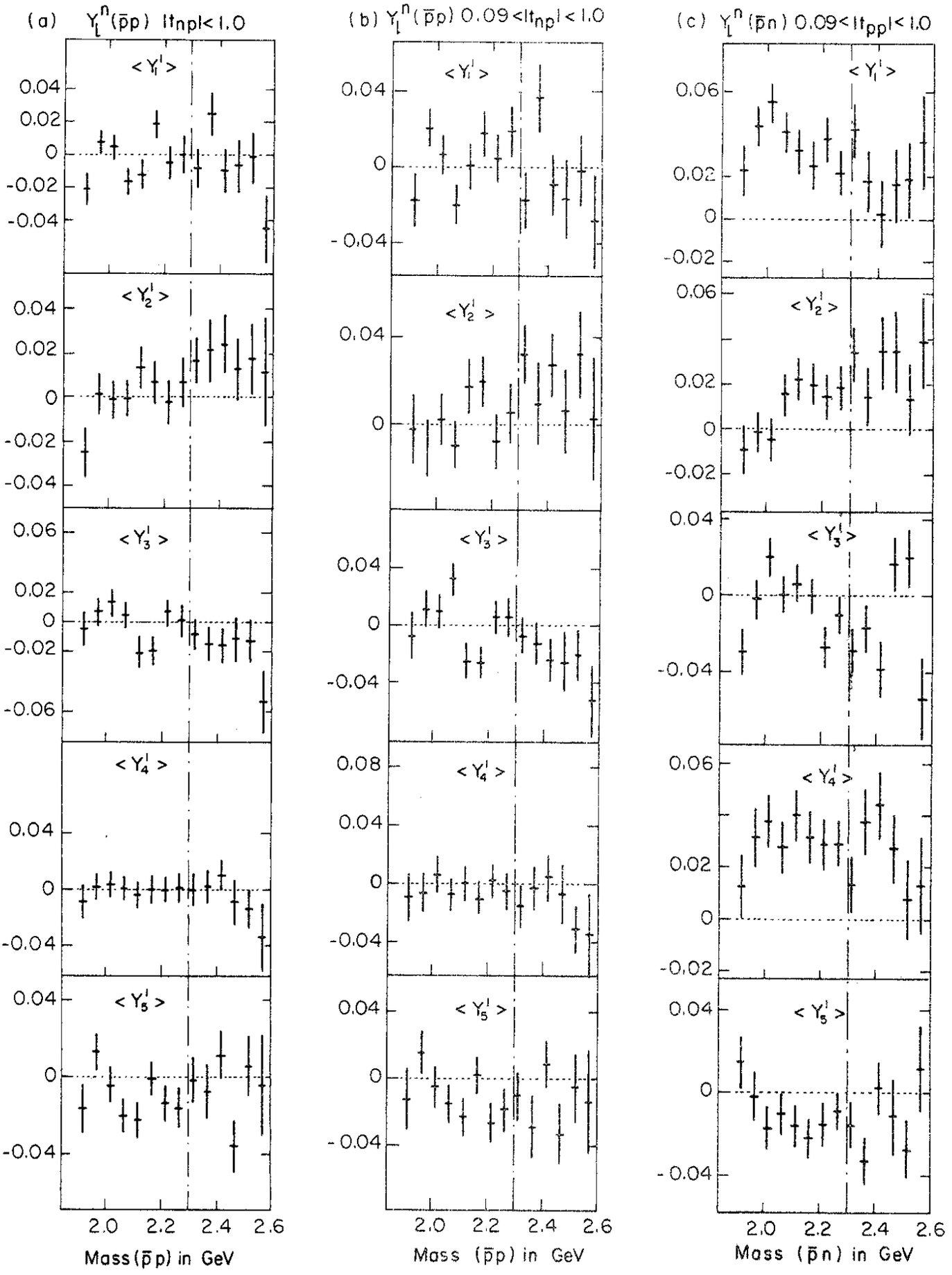
(a) $Y_L^n(\bar{p}p)$ $|t_{np}|<1.0$
(b) $Y_L^n(\bar{p}p)$ $0.09<|t_{np}|<1.0$
(c) $Y_L^n(\bar{p}n)$ $0.09<|t_{pp}|<1.0$
$\langle Y_1^l \rangle$
$\langle Y_2^l \rangle$
$\langle Y_3^l \rangle$
$\langle Y_4^l \rangle$
$\langle Y_5^l \rangle$
Mass $(\bar{p}p)$ in GeV
Mass $(\bar{p}p)$ in GeV
Mass $(\bar{p}n)$ in GeV

Fig. 10

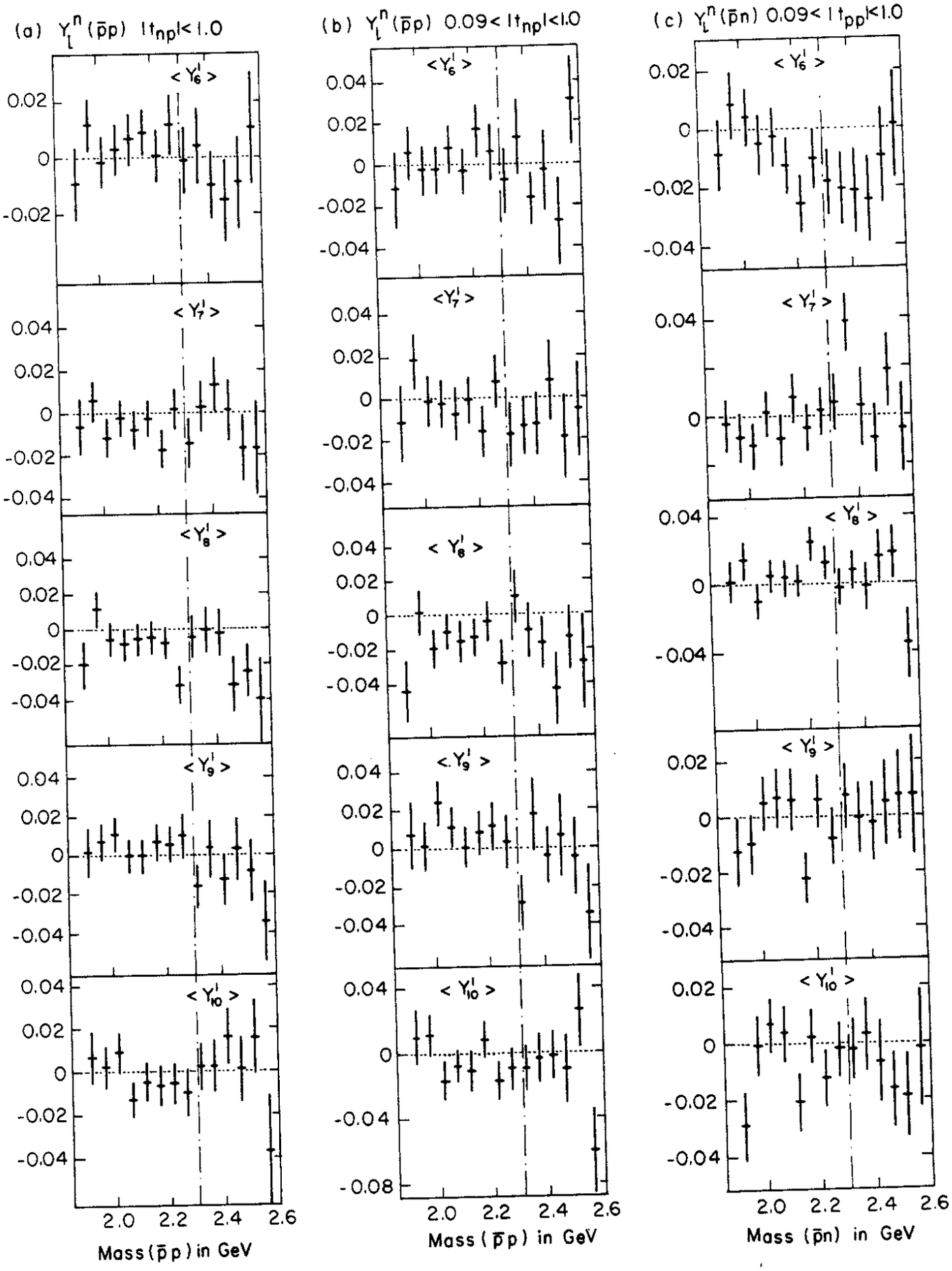
(a) $Y_L^n(\bar{p}p)$ $|t_{np}|<1.0$
(b) $Y_L^n(\bar{p}p)$ $0.09<|t_{np}|<1.0$
(c) $Y_L^n(\bar{p}n)$ $0.09<|t_{pp}|<1.0$
$\langle Y_6^1 \rangle$
$\langle Y_7^1 \rangle$
$\langle Y_8^1 \rangle$
$\langle Y_9^1 \rangle$
$\langle Y_{10}^1 \rangle$
Mass $(\bar{p}p)$ in GeV
Mass $(\bar{p}p)$ in GeV
Mass $(\bar{p}n)$ in GeV

Fig. 11